Supplement of Weather Clim. Dynam., 6, 879–899, 2025
https://doi.org/10.5194/wcd-6-879-2025-supplement

Supplement of

Physical processes leading to extreme day-to-day temperature change – Part 1: Present-day climate

Kalpana Hamal and Stephan Pfahl

Correspondence to: Kalpana Hamal (k.hamal@fu-berlin.de)

Supplementary File

Observations datasets

HadGHCND is a gridded daily temperature data set that includes near-surface minimum and maximum temperature data from 1950 to the present, developed by the National Centers for Environmental Information. It is based on meticulously quality-controlled observations from ~27,000 global stations within the Global Historical Climatology Network daily database (Caesar et al., 2006). The data have been interpolated on a 2.5° latitude by 3.75° longitude grid, employing an angular distance weighting scheme for spatial consistency. Specifically designed to analyze climate extremes and climate model evaluation, the dataset offers temperature anomalies (based on a 1961-1990 climatology) and actual temperatures separately. Given its comprehensive nature and rigorous quality control, the HadGHCND data provide a robust foundation for global climatic studies (Wan et al., 2021; Xu et al., 2020). For the current study, we used global daily HadGHCND minimum and maximum temperatures from 1980 to 2014 and then calculated the daily mean temperature.

The Berkeley Earth Surface Temperatures (BEST) dataset provides a long-term, high-resolution record of global temperatures, covering land from 1701 to the present, developed by the Berkeley Earth project (Rohde and Hausfather, 2020). It integrates approximately 39,000 station records, incorporating additional data sources beyond HadGHCND. The dataset offers mean temperature, minimum temperature, and maximum temperature at a daily timescale with a horizontal resolution of 1° × 1°. The BEST gridded observation dataset has already been extensively applied to study temperature extremes and to validate results with reanalysis datasets (Rantanen et al., 2022; Russo and Domeisen, 2023). We used the available daily mean temperature data from 1980 to 2020 for this study.

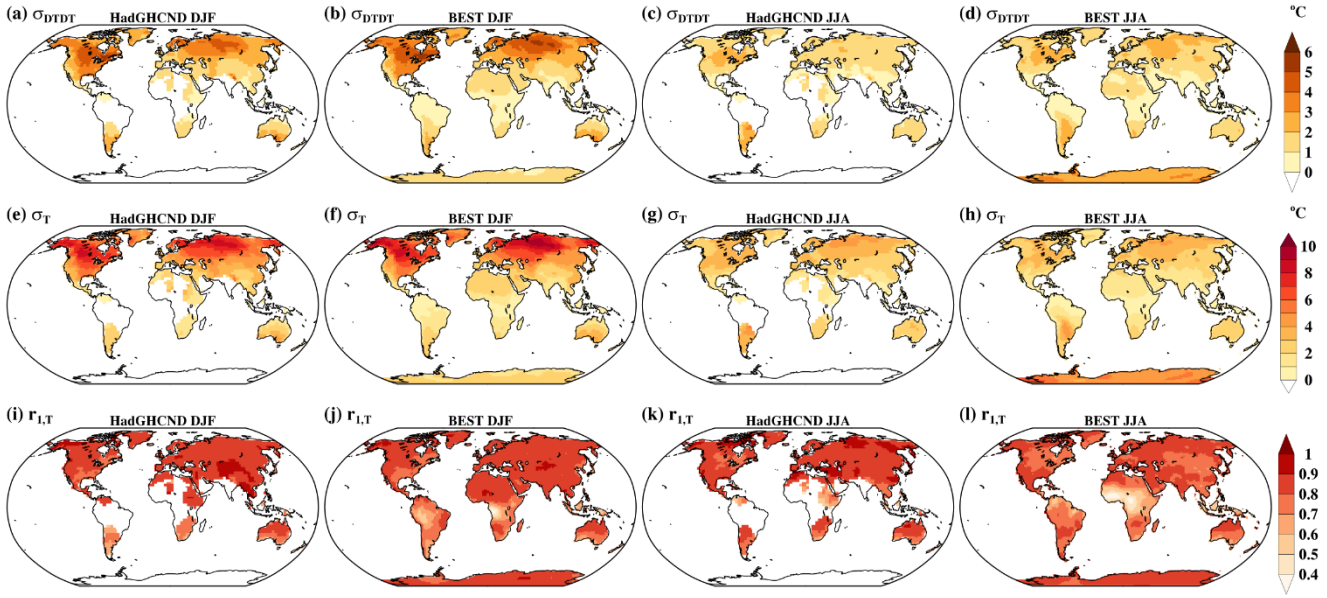

Figure S1. (**a-d**) The standard deviation of DTDT variations (σ_{DTDT}; °C), (**e-h**) the standard deviation of daily mean temperature (σ_T; °C), and (**i-l**) the lag-1 autocorrelation of daily mean temperature ($r_{1,T}$) in December-February (DJF) and June-August (JJA) as derived from the HadGHCND and BEST datasets.

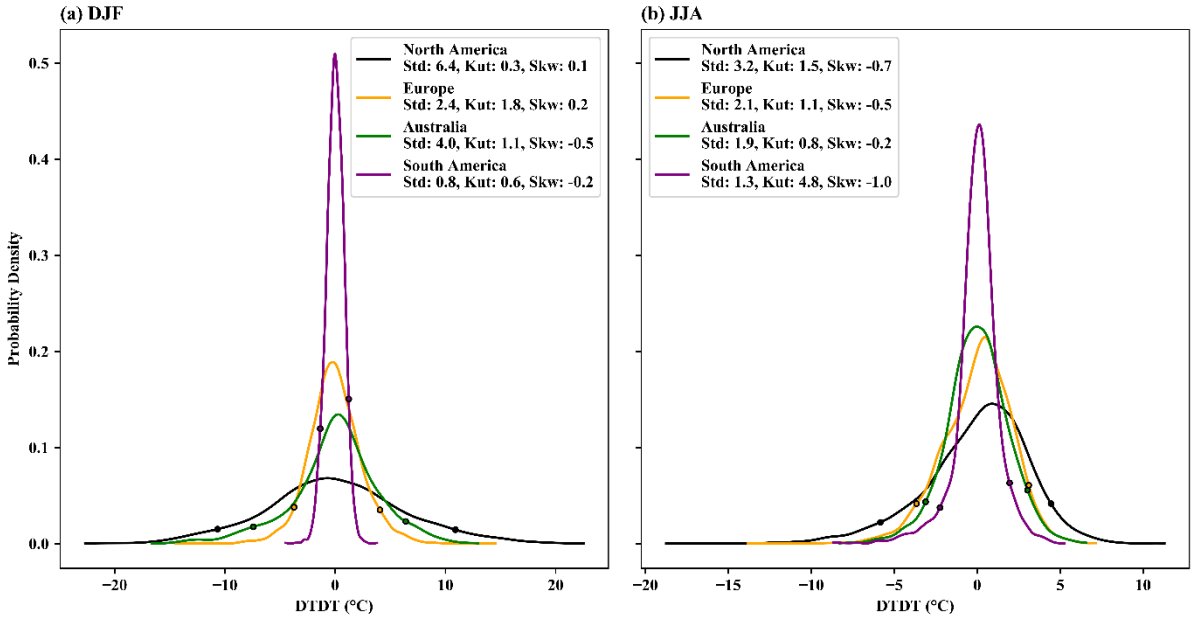

Figure S2. The day-to-day temperature (DTDT; °C) distribution curves over the selected locations: North America (black), Europe (orange), Australia (green), and South America (magenta) for (**a**) December-February (DJF) and (**b**) June-August (JJA). The small dots on the left and right represent the 5th and 95th percentiles, respectively.

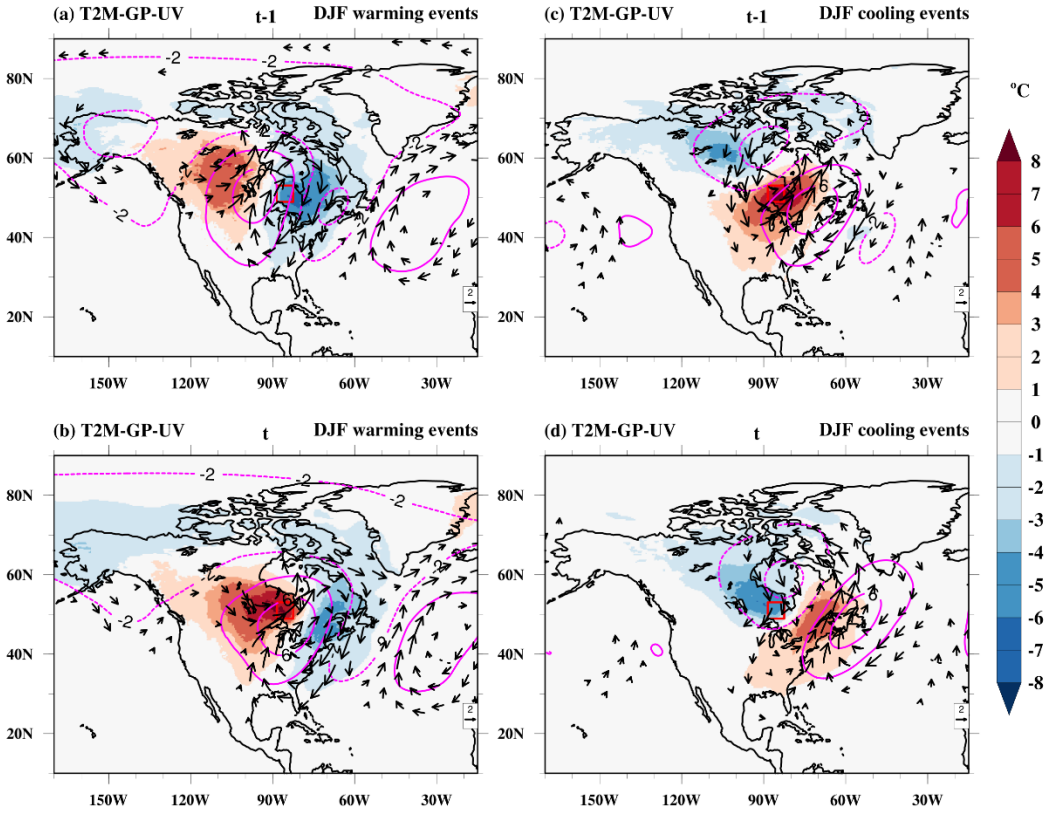

Figure S3. Composite of near-surface temperature anomalies (T2M; °C, color shading), wind anomalies at 850 hPa (UV; m s^{-1}, vectors), and geopotential height anomalies at 500 hPa (GP; gpm, magenta contours, dotted and bold magenta contours show negative and positive values, respectively) with respect to seasonal mean on (**a, c**) the previous day (*t*-1) and (**b, d**) the event day (*t*) of the warming (**a, b**) and cooling (**c, d**) events during December-February (DJF) at a selected grid box in North America (red box). Note that wind vector anomalies ≥ 2 m s^{-1} are plotted.

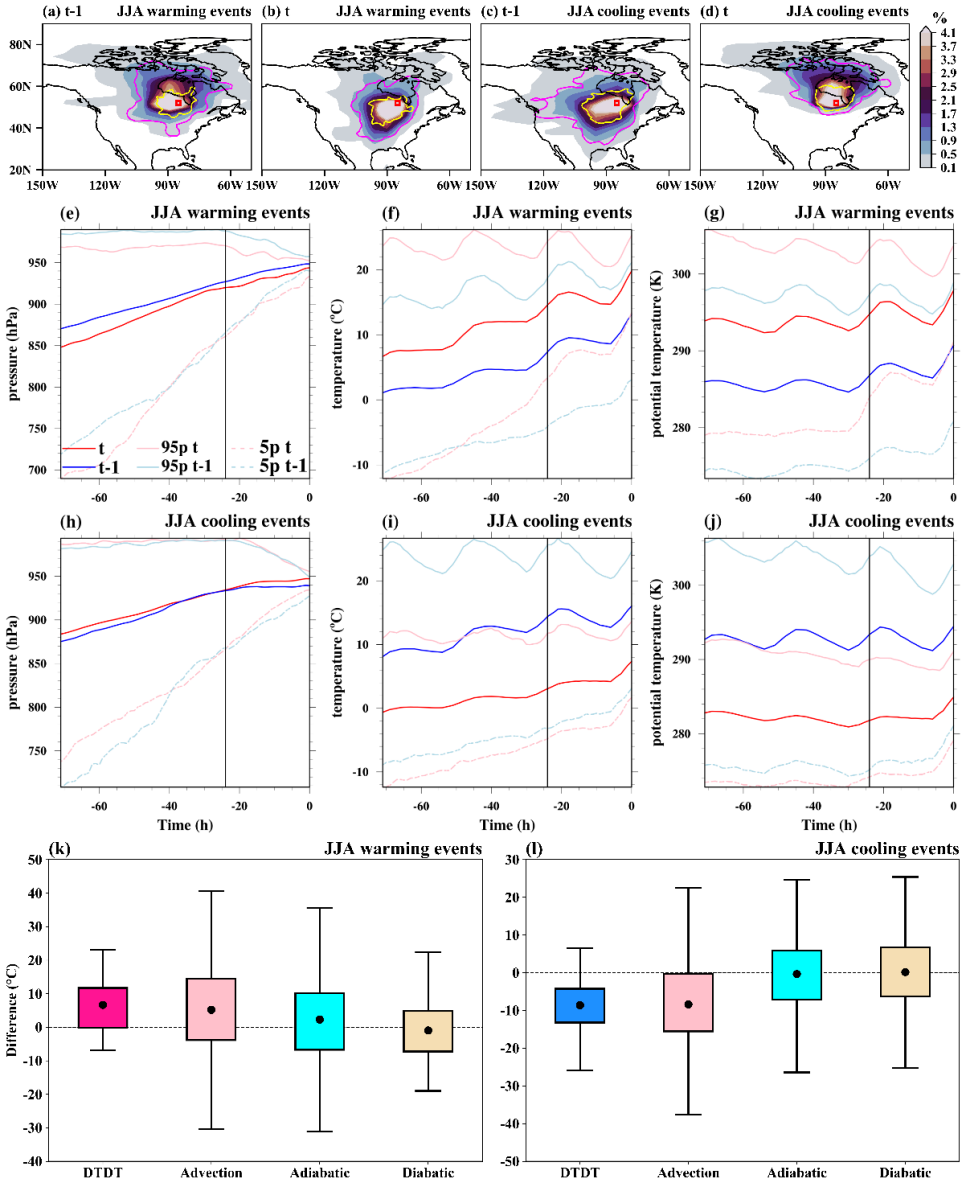

Figure S4. The spatial distribution of trajectories initiated on the previous day ($t-1$) and on the event day (t) for June-August (JJA) warming and cooling events over North America. In the top row, the color shading illustrates the air parcel trajectory density (%) based on the position between −5 and 0 d. The magenta and yellow contours represent 0.5 % particle density fields at −3 and −1 d, respectively. The red box shows the selected grid box over North America. The Lagrangian evolution of distinct physical parameters (pressure, temperature, potential temperature) along the air parcel trajectories for both warming (second row) and cooling events (third row) is presented in panels **(e)**–**(j).** Panels **(k)** and **(l)** show the contribution of the different physical processes to the genesis of extreme DTDT changes according to Eq. (6), which refers to a 3 d timescale. The box spans the 25th and 75th percentiles of the data; the black dot inside the box gives the mean of the related quantities; and 1.5 times the interquartile range is indicated by the whiskers.

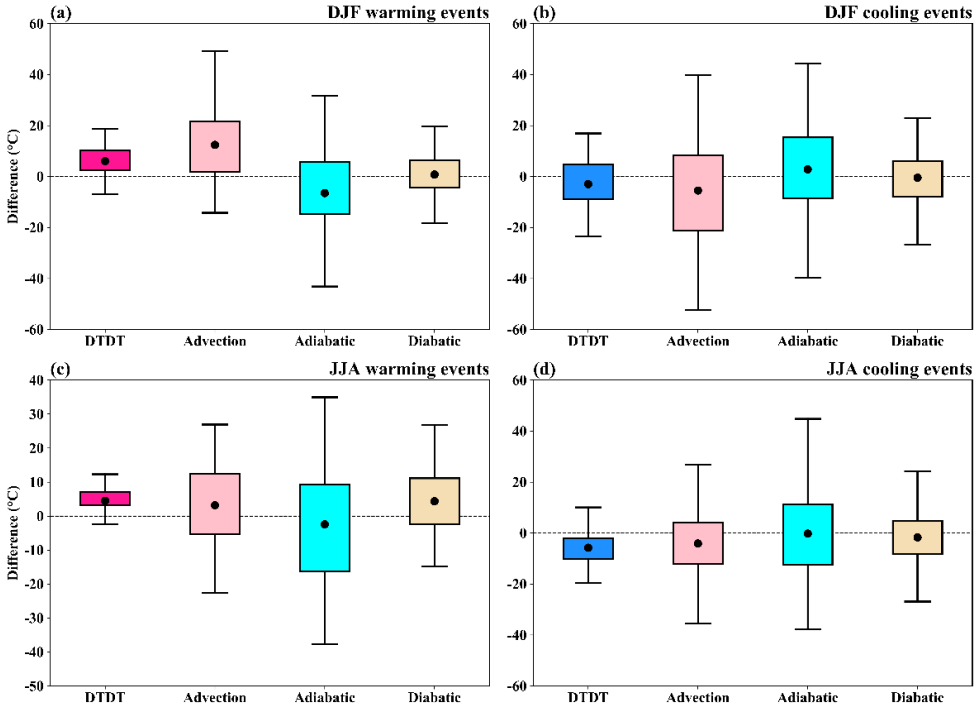

Figure S5. The contribution of the different physical processes (advection, adiabatic, and diabatic) to the genesis of extreme DTDT changes over mid-latitudes: western North America, according to Eq. (6), which refers to a 3 d timescale during **(a, b)** December-February (DJF) and **(c, d)** June-August (JJA). The box spans the 25th and 75th percentiles of the data; the black dot inside the box gives the mean of the related quantities; and 1.5 times the interquartile range is indicated by the whiskers.

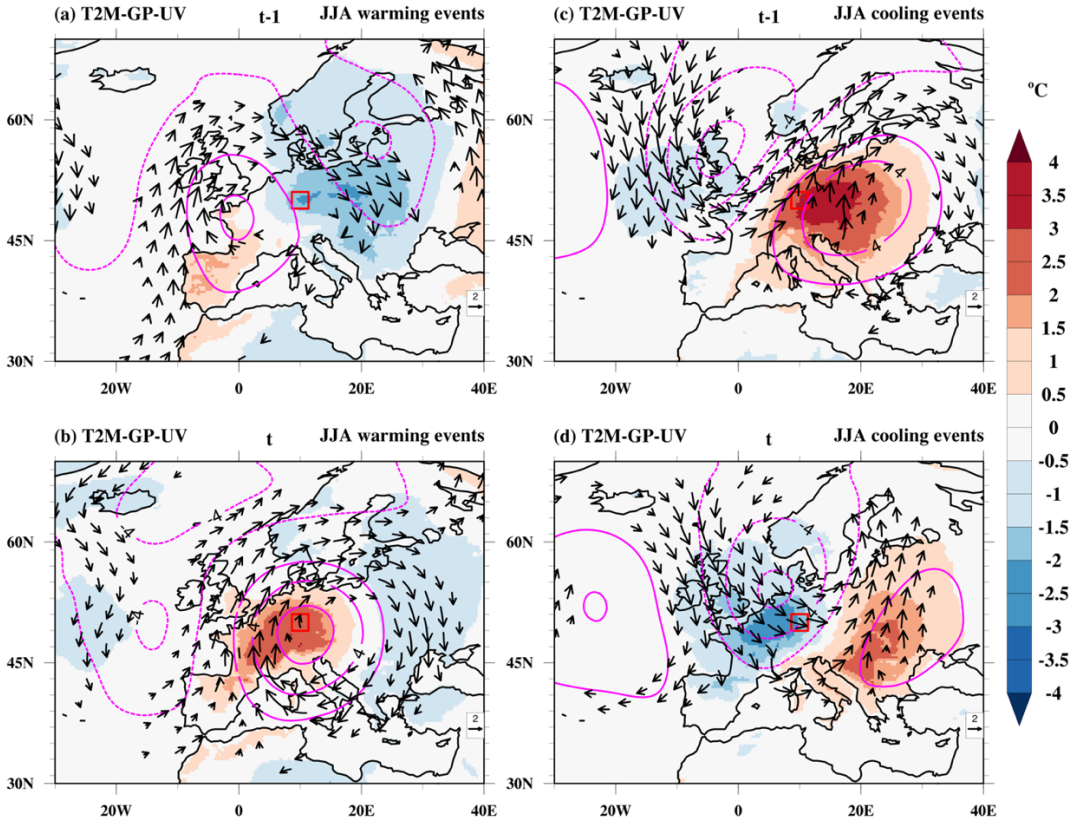

Figure S6. Composite of near-surface temperature anomalies (T2M; °C, color shading), wind anomalies at 850 hPa (UV; m s^{-1}, vectors), and geopotential height anomalies at 500 hPa (GP; gpm, magenta contours, dotted and bold magenta contours show negative and positive values, respectively) with respect to seasonal mean on **(a, c)** the previous day (*t*-1) and **(b, d)** the event day (*t*) of the warming **(a, b)** and cooling **(c, d)** events during June-August (JJA) at a selected grid box in Europe (red box). Note that wind vector anomalies ≥ 2 m s^{-1} are plotted.

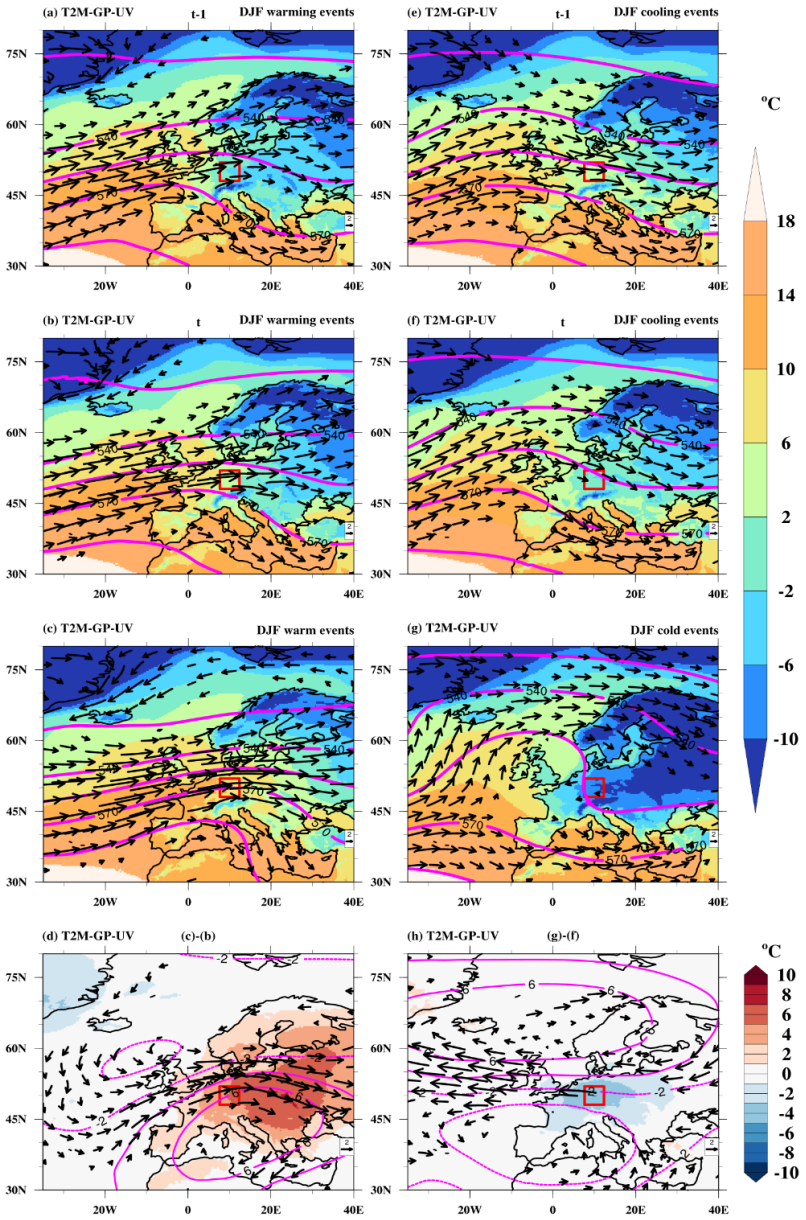

Figure S7. Composite of near-surface temperature (T2M; °C, color shading), wind at 850 hPa (UV; m s^{-1}, vectors), and Geopotential height at 500 hPa (GP; gpm, magenta contours) on **(a, e)** the previous day (*t*-1) and **(b, f)** the event day (*t*) of warming **(a-b)** and cooling **(e-f)** events during December-February (DJF) at a selected grid box in Europe (red box). Composites of **(c)** warm and **(g)** cold events, defined as events with 5th and 95th percentiles of the daily temperature distribution as thresholds, are shown in the third row, and the difference between daily extremes (panels **c** and **g**) and DTDT extremes (panels **b** and **f**) are shown in panels **(d)** and **(h)**. Note that in (**a-c** and **e-g**), wind vectors ≥ 3 m s^{-1}, and in (**d and h**), wind vector anomalies ≥ 1 m s^{-1} are plotted. The dotted and bold magenta contours in **(d)** and **(h)** indicate negative and positive values of geopotential height differences, respectively.

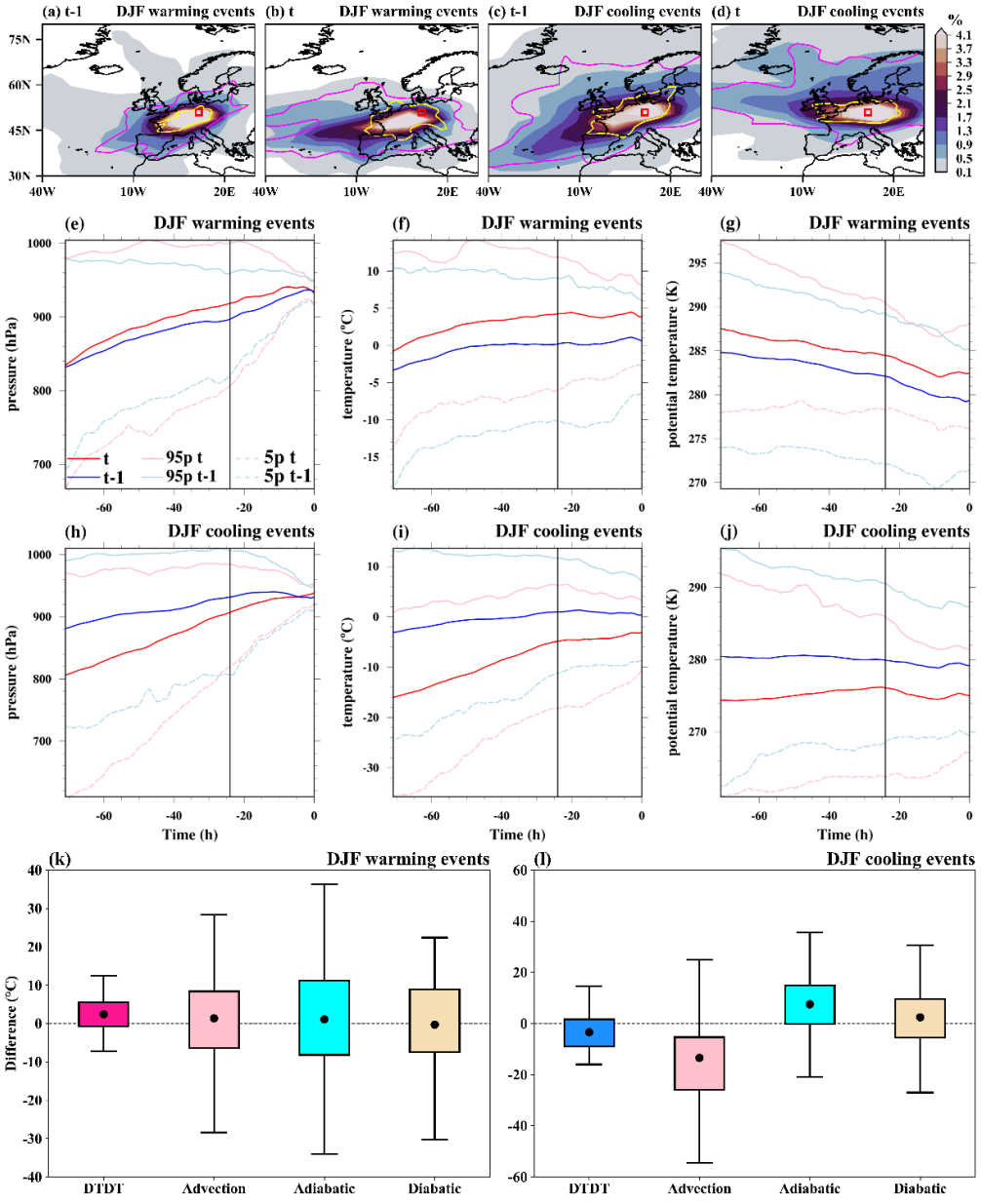

Figure S8. The spatial distribution of trajectories initiated on the previous day ($t-1$) and on the event day (t) for both December-February (DJF) warming and cooling events over Europe. In the top row, the color shading illustrates the air parcel trajectory density (%) based on the position between −5 and 0 d. The magenta and yellow contours represent 0.5 % particle density fields at −3 and −1 d, respectively. The red box shows the selected grid box over Europe. The Lagrangian evolution of distinct physical parameters (pressure, temperature, potential temperature) along the air parcel trajectories for both warming (second row) and cooling events (third row) is presented in panels **(e)–(j).** Panels **(k)** and **(l)** show the contribution of the different physical processes to the genesis of extreme DTDT changes according to Eq. (6), which refers to a 3 d timescale. The box spans the 25th and 75th percentiles of the data; the black dot inside the box gives the mean of the related quantities; and 1.5 times the interquartile range is indicated by the whiskers.

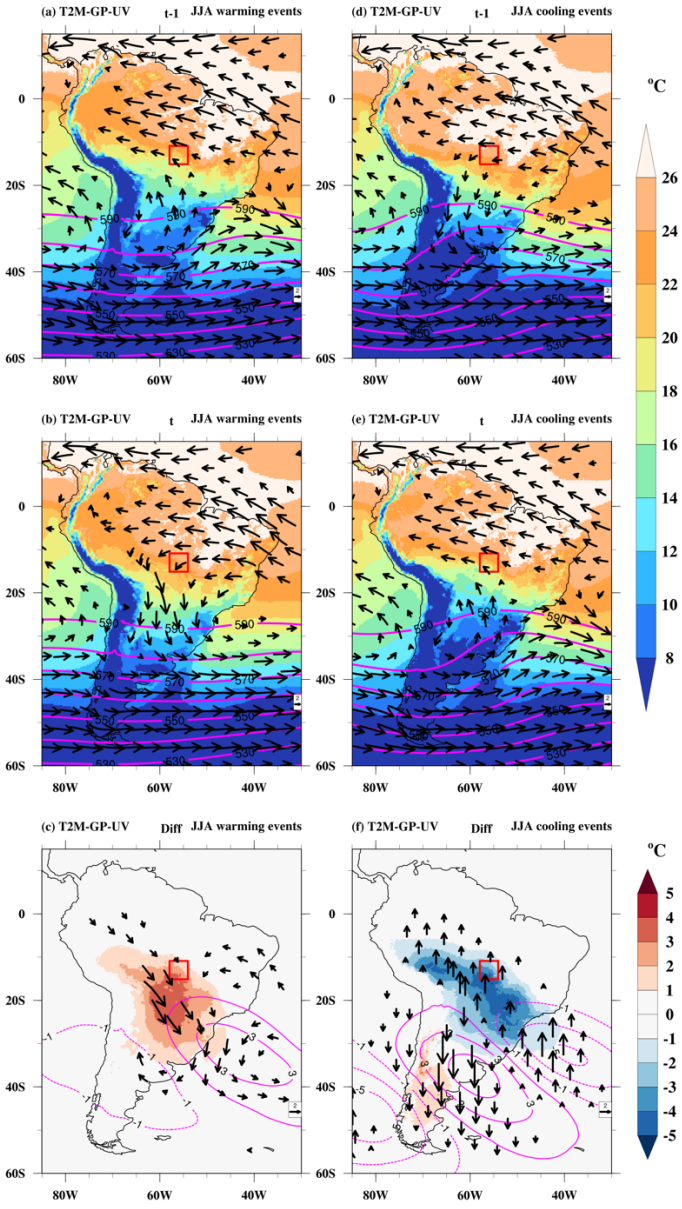

90 **Figure S9.** Composite of near-surface temperature (T2M; °C, color shading), wind at 850 hPa (UV; m s^{-1}, vectors), and geopotential height at 500 hPa (GP; gpm, magenta contours) on **(a, d)** the previous day ($t-1$) and **(b, e)** the event day (t) and **(c, f)** the difference (diff) between the event day and the previous day of the warming **(a–c)** and cooling **(d–f)** events during June-August (JJA) at a selected grid box in South America (red box). Note that in (**a–b** and **d–e**) wind vectors ≥ 2 m s^{-1} and in (**c, f**) wind anomalies ≥ 1 m s^{-1} are plotted. The dotted and bold magenta contours in (**c**) and (**f**) indicate negative and positive geopotential height differences, respectively.

95

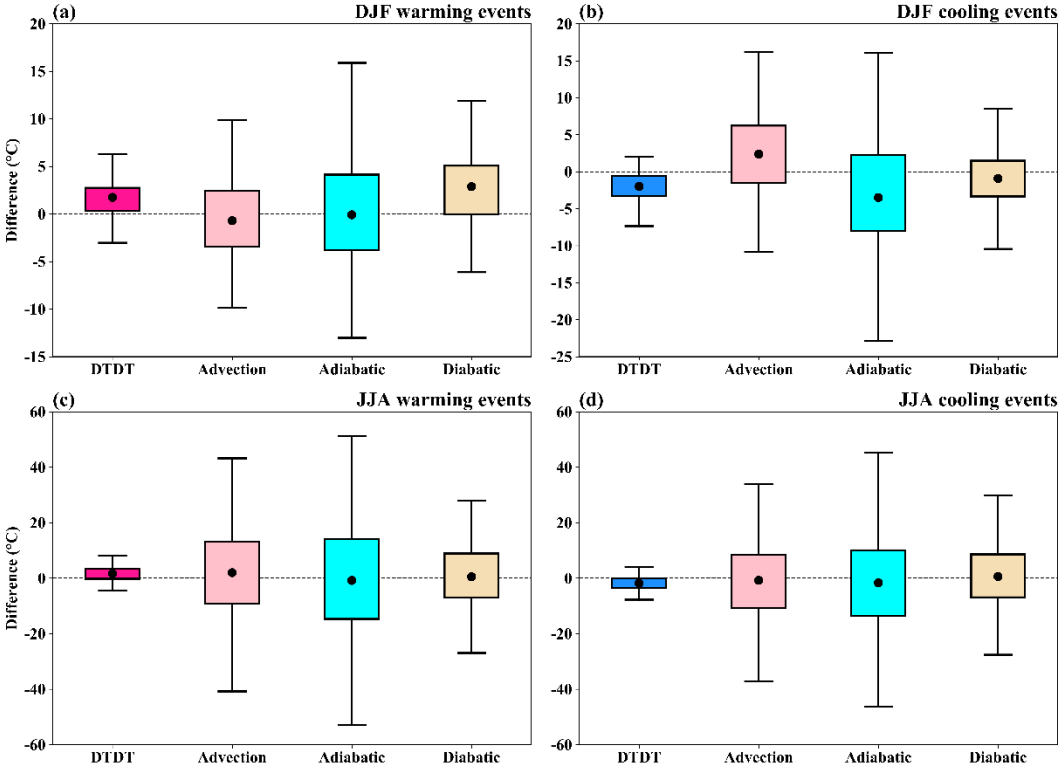

Figure S10. The contribution of the different physical processes (advection, adiabatic, and diabatic) to the genesis of extreme DTDT changes over Tropics: Southern Africa, according to Eq. (6), which refers to a 3 d timescale during **(a, b)** December-February (DJF) and **(c, d)** June-August (JJA). The box spans the 25th and 75th percentiles of the data; the black dot inside the box gives the mean of the related quantities; and 1.5 times the interquartile range is indicated by the whiskers.

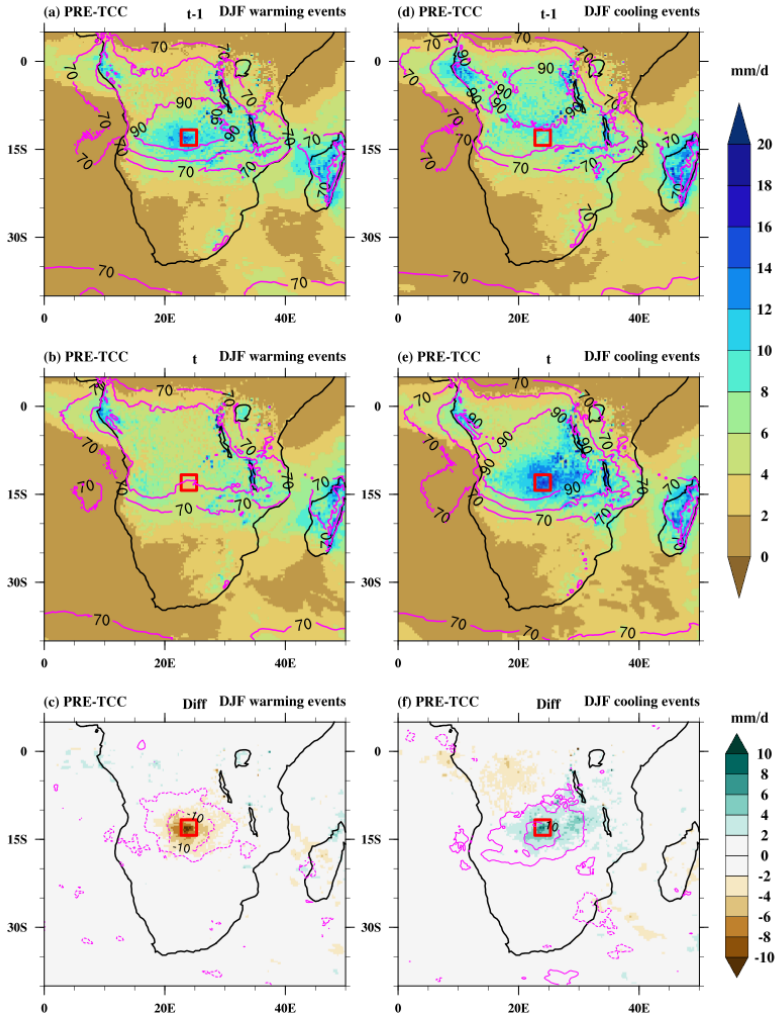

Figure S11. Composites of precipitation (PRE; mm d^{-1}, color shading) and total cloud cover (TCC; %, magenta contours) on **(a, d)** the previous day ($t-1$) and **(b, e)** the event day (t) and **(c, f)** the difference (diff) between the event day and the previous day of the warming **(a–c)** and cooling **(d–f)** events during December–February (DJF) at a selected grid box in Southern Africa (red box). The dotted and bold magenta contours in **(c)** and **(f)** indicate negative and positive total cloud cover differences, respectively.

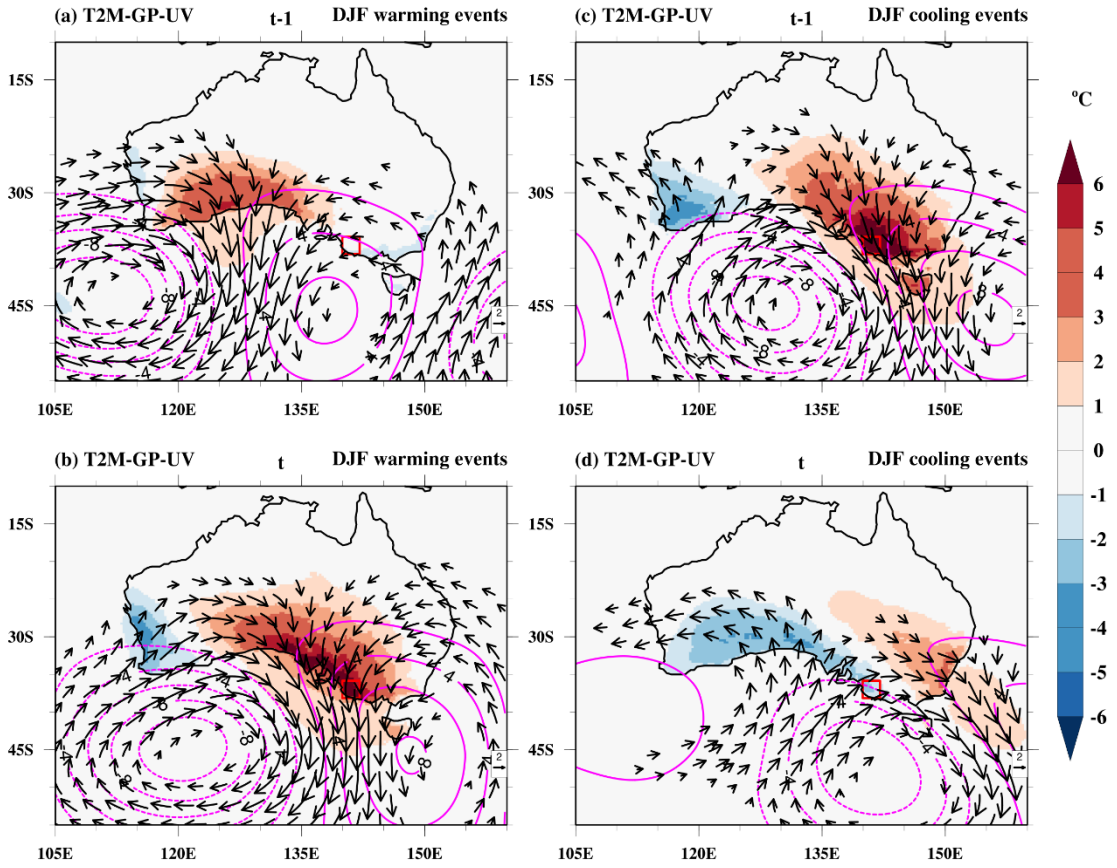

Figure S12. Composite of near-surface temperature anomalies (T2M; °C, color shading), wind anomalies at 850 hPa (UV; m s^{-1}, vectors), and geopotential height anomalies at 500 hPa (GP; gpm, magenta contours, dotted and bold magenta contours show negative and positive values, respectively) with respect to seasonal mean on **(a, c)** the previous day (*t*-1) and **(b, d)** the event day (*t*) of the warming **(a, b)** and cooling events **(c, d)** during December-February (DJF) at a selected grid box in Australia (red box). Note that wind vector anomalies ≥ 2 m s^{-1} are plotted.

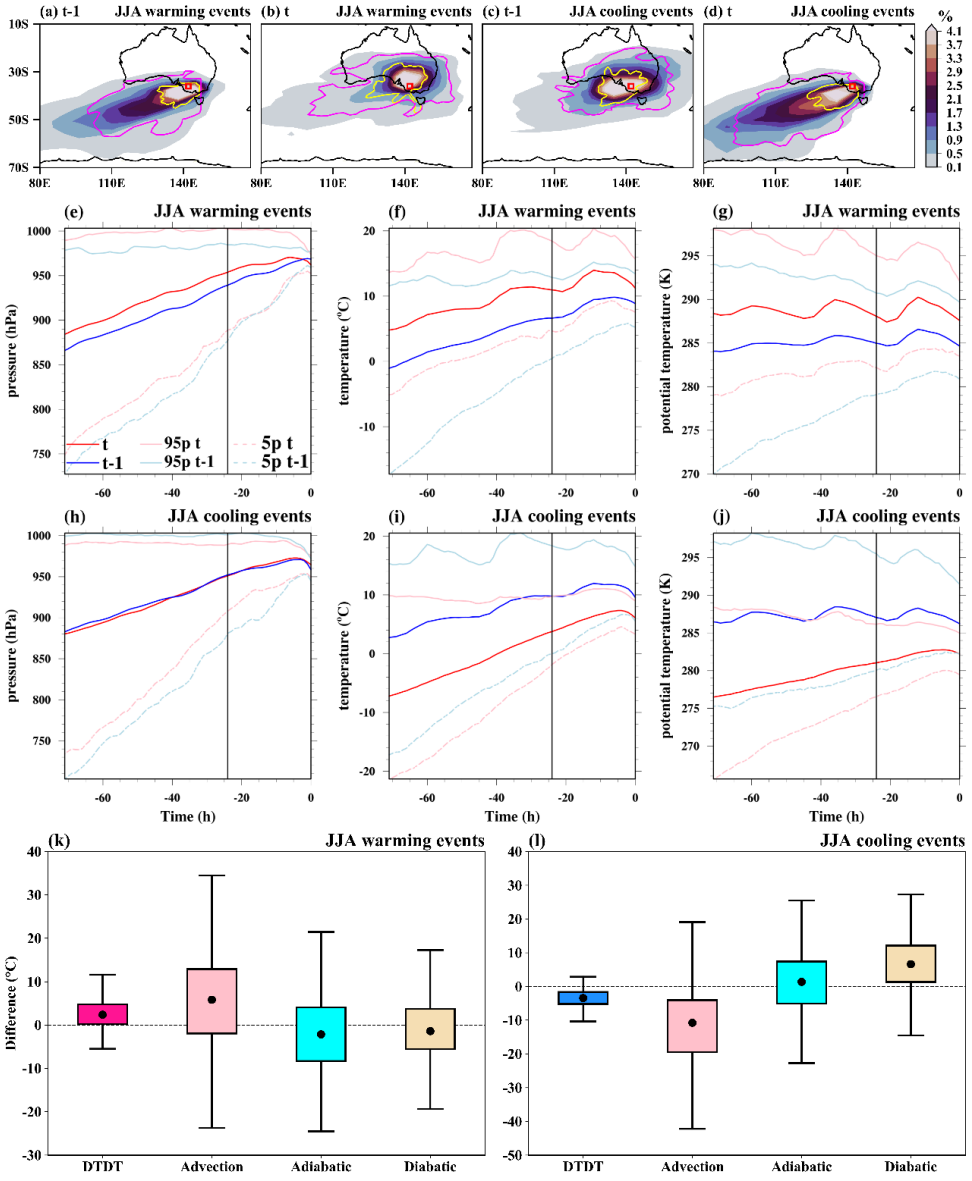

Figure S13. The spatial distribution of trajectories initiated on the previous day ($t-1$) and on the event day (t) for June-August (JJA) warming and cooling events over Australia. In the top row, the color shading illustrates the air parcel trajectory density (%) based on the position between −5 and 0 d. The magenta and yellow contours represent 0.5 % particle density fields at −3 and −1 d, respectively. The red box shows the selected grid box over Australia. The Lagrangian evolution of distinct physical parameters (pressure, temperature, potential temperature) along the air parcel trajectories for both warming (second row) and cooling events (third row) is presented in panels **(e)–(j)**. Panels **(k)** and **(l)** show the contribution of the different physical processes to the genesis of extreme DTDT changes according to Eq. (6), which refers to a 3 d timescale. The box spans the 25th and 75th percentiles of the data; the black dot inside the box gives the mean of the related quantities; and 1.5 times the interquartile range is indicated by the whiskers.

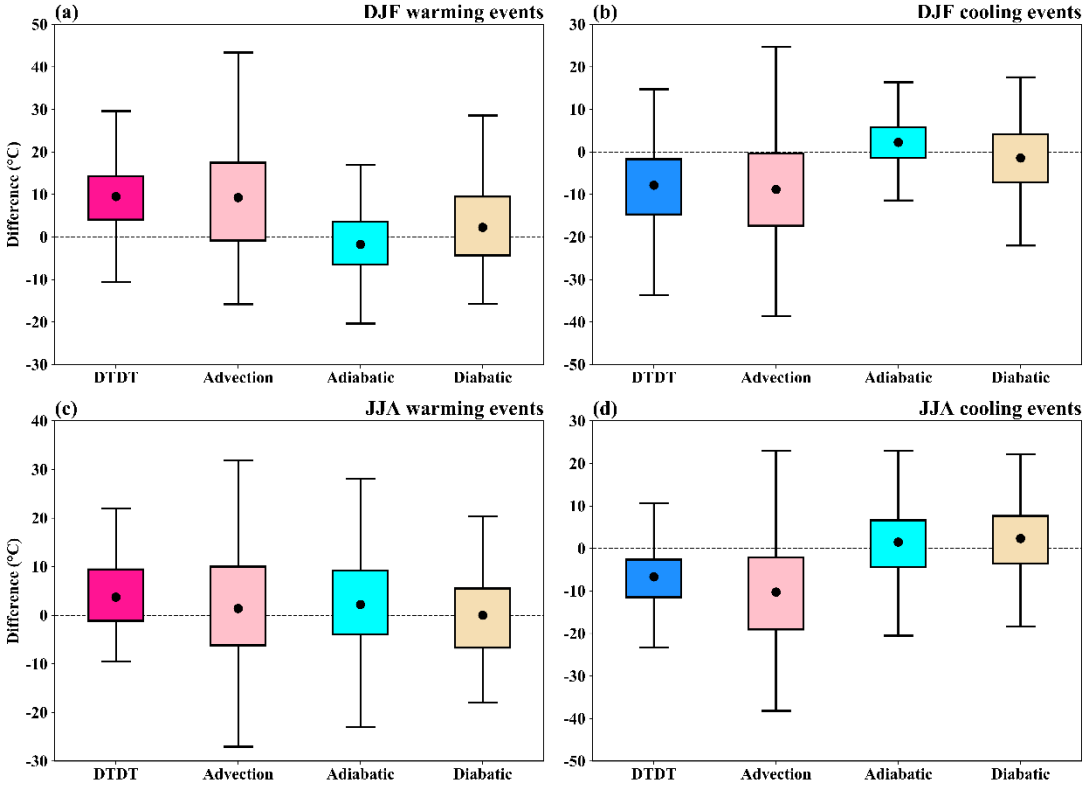

Figure S14. The contribution of the different physical processes (advection, adiabatic, and diabatic) to the genesis of extreme DTDT changes over high latitudes: Northern Asia, according to Eq. (6), which refers to a 3 timescale during **(a, b)** December-February (DJF) and **(c, d)** June-August (JJA). The box spans the 25th and 75th percentiles of the data; the black dot inside the box gives the mean of the related quantities; and 1.5 times the interquartile range is indicated by the whiskers.

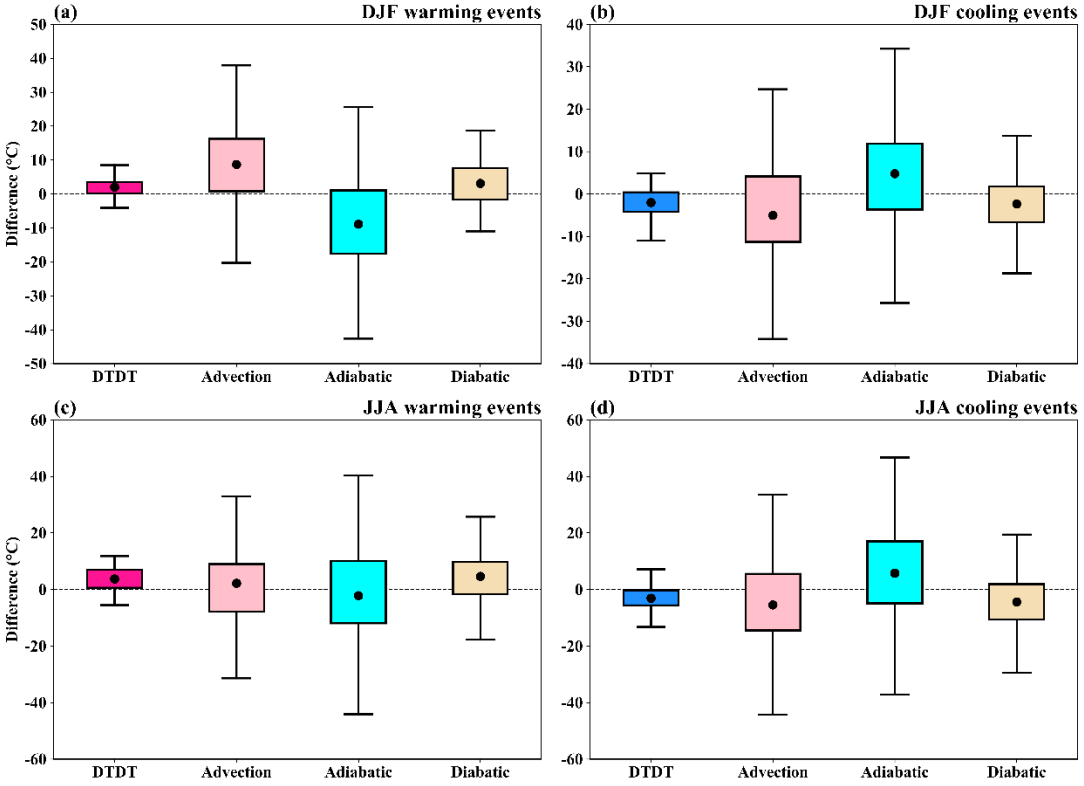

Figure S15. The contribution of the different physical processes (advection, adiabatic, and diabatic) to the genesis of extreme DTDT changes over sub-tropics: Southern Asia, according to Eq. (6), which refers to a 3 d timescale during **(a, b)** December-February (DJF) and **(c, d)** June-August (JJA). The box spans the 25th and 75th percentiles of the data; the black dot inside the box gives the mean of the related quantities; and 1.5 times the interquartile range is indicated by the whiskers.

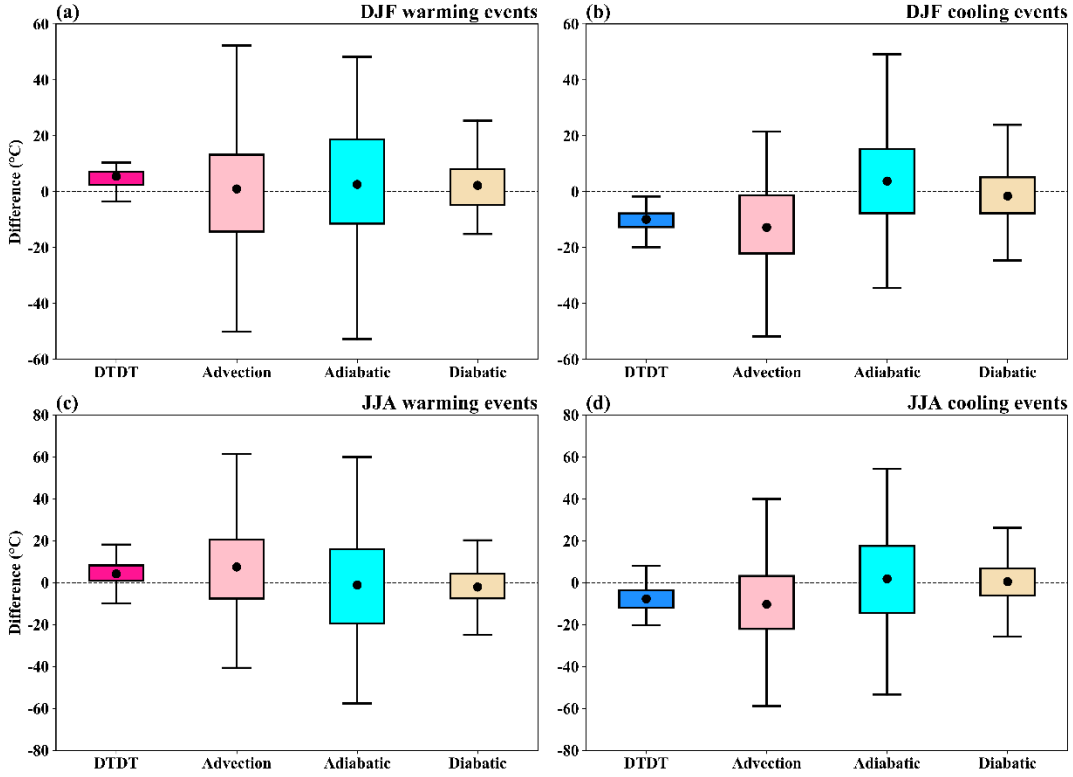

Figure S16. The contribution of the different physical processes (advection, adiabatic, and diabatic) to the genesis of extreme DTDT changes over mid-latitudes: Southern South America, according to Eq. (6), which refers to a 3 d timescale during **(a, b)** December-February (DJF) and **(c, d)** June-August (JJA). The box spans the 25th and 75th percentiles of the data; the black dot inside the box gives the mean of the related quantities; and 1.5 times the interquartile range is indicated by the whiskers.

References

Caesar, J., Alexander, L., and Vose, R.: Large-scale changes in observed daily maximum and minimum temperatures: Creation and analysis of a new gridded data set [data set], J. Geophys. Res., 111, D05101, https://doi.org/10.1029/2005JD006280, 2006.

Rantanen, M., Karpechko, A. Y., Lipponen, A., Nordling, K., Hyvärinen, O., Ruosteenoja, K., Vihma, T., and Laaksonen, A.: The Arctic has warmed nearly four times faster than the globe since 1979, Communications earth & environment, 3, 168, https://doi.org/10.1038/s43247-022-00498-3, 2022.

Rohde, R. A., and Hausfather, Z.: The Berkeley Earth Land/Ocean Temperature Record [data set], Earth Syst. Sci. Data, 12, 3469–3479, https://doi.org/10.5194/essd-12-3469-2020, 2020.

Russo, E. and Domeisen, D. I.: Increasing intensity of extreme heatwaves: The crucial role of metrics, Geophysical Research Letters, 50, e2023GL103540, https://doi.org/10.1029/2023GL103540, 2023.

Wan, H., Kirchmeier-Young, M., and Zhang, X.: Human influence on daily temperature variability over land, Environmental Research Letters, 16, 094026, https://doi.org/10.1088/1748-9326/ac1cb9, 2021.

Xu, Z., Huang, F., Liu, Q., and Fu, C.: Global pattern of historical and future changes in rapid temperature variability, Environmental Research Letters, 15, 124073, https://doi.org/10.1088/1748-9326/abccf3, 2020.